

Article

# Single-Phase Bidirectional On-Board Charger Using Starter Generator System in Hybrid Electric Vehicles

Seok-Min Kim, Ho-Sung Kang and Kyo-Beum Lee \* 

Department of Electrical and Computer Engineering, Ajou University, 206, World cup-ro, Yeongtong-gu, Suwon 16499, Korea; smkim@ajou.ac.kr (S.-M.K.); fgrtoy11@ajou.ac.kr (H.-S.K.)

\* Correspondence: kyl@ajou.ac.kr; Tel.: +82-31-219-2376

Received: 6 October 2018; Accepted: 28 October 2018; Published: 1 November 2018



**Abstract:** This paper presents the design and control methods of a single-phase bidirectional on-board charger (OBC) using a hybrid starter generator (HSG) and an inverter in a hybrid electric vehicle (HEV). In an HEV, there are a number of components, including the combustion engine, transmission, traction motor, motor controller, OBC, and HSG system. The proposed design reconfigures the HSG system to provide battery-charging capability instead of a conventional OBC based on the use of additional power relays. As a result, the number of power converters is effectively reduced through the replacement of the conventional OBC, and, thus, the power density is increased. This paper also proposes a control method for enabling not only battery charging but also a reactive power support depending on the grid command. Compared with a conventional reactive power compensation method, the proposed method has an advantage because it is located near the principal reactive power source. The simulation and experimental results verify the validity and feasibility of the proposed bidirectional OBC design and its control methods.

**Keywords:** hybrid electric vehicles (HEVs); bidirectional on-board charger (OBC); grid to vehicle (G2V); vehicle to grid (V2G); hybrid starter generator (HSG) system; reactive power support

## 1. Introduction

With growing concerns regarding environmental contamination and global warming, a principal conversion of innovative technology has occurred, moving from conventional internal combustion engine (ICE) powered vehicles to more energy-efficient vehicles, including electric vehicles (EVs) and hybrid EVs (HEVs). Typically, ICE-powered vehicles have certain disadvantages, such as low driving efficiency and excessive emissions of environmental pollutants. However, there are still technical limitations to the active use of pure EVs, including a lack of charging infrastructure and a limited driving range owing to low battery performance. As a result, HEVs can be a compromise compensating the limitations of conventional ICE-powered vehicles and EVs [1–5]. Accordingly, many studies regarding a more efficient driving style for HEVs, such as exploiting the essential configuration of the vehicle, have been conducted globally [6–10].

Owing to the use of dual power sources, HEVs are composed of various mechanical and electrical components, such as a combustion engine, electrical traction motor, transmission, battery, power converters, and battery charger (OBC). In addition, HEVs include a hybrid starter generator (HSG) system composed of the HSG and its drive inverter for starting the engine from an idle stop and eliminating exhaust gas emissions when the vehicle is stopped temporarily [11–13]. Furthermore, the HSG system is also used to charge the battery through the use of regenerative braking, which converts the kinetic energy of the vehicle into electric energy [14].

There are various circuit configurations and control strategies for the battery charging [15–17]. In this paper, a novel integrated charging circuit is proposed. The circuit of the HSG system is

reconstructed through the operation of relays and an additional circuit as shown in Figure 1. Thus, the HSG system provides a conventional operation and bidirectional OBC by changing the switching states of the relays. The proposed circuit design substitutes for the conventional OBC, and, thus, the conventional OBC can be eliminated from the HEV. As a result, the integrated charging system results decrease of the required volume and weight of the entire system along with the manufacturing costs for the power components. The reduction in components implies an increase in power density.

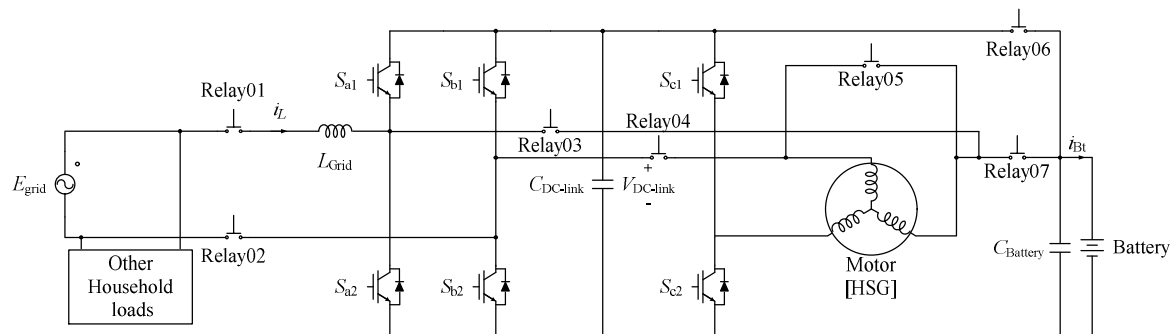


**Figure 1.** Proposed circuit for hybrid starter generator (HSG) driving and single-phase bidirectional on-board charger (OBC).

Because most vehicles are parked for more than 85% of their lifespan, studies are being actively conducted on utilizing the OBC of an HEV and the battery storage [18,19]. In general, many of these studies have concentrated on a conventional bidirectional OBC, which only allows an active power flow from the grid to vehicle (G2V) and vehicle to grid (V2G). In contrast, we propose a control method for charging the battery and compensating the reactive power simultaneously through the use of the modified HSG system. Compared with conventional methods for compensation of the reactive power, the proposed reactive power control method is suitable and efficient for the residential charging of the HEV because the vehicle is located next to the residential area.

By increasing the number of distributed generation systems, the problems from the DC offset and low-order harmonics in the grid current become more severe. The DC offset component saturates the distribution transformers, resulting in waveform distortion, excessive losses, and overheating [20,21]. In addition, low-order harmonics affect the capacitor bank failure, over-voltages, and aggravation of the control performance [22,23]. Therefore, the proposed control method includes a DC offset and low-order harmonics compensators for improving the quality of the grid current. The DC offset component and low-order harmonics are extracted through a coordinate transformation without the use of additional sensors and are effectively eliminated.

The simulation and experimental results verify the validity and feasibility of the proposed single-phase bidirectional OBC design and its control method. A practical experiment was conducted using a 6.5 kW rated single-phase bidirectional OBC prototype.

## 2. Proposed HSG Circuit and Operating Mode

In general, a conventional HEV consists of an HSG, its drive inverter, battery, and OBC. A separate system configuration causes an increase in the system volume and weight, leading to a reduction in the power system density of the overall system in the HSG.

Figure 1 shows the proposed integrated circuit configuration enabling the battery charging functionality of the conventional OBC as well as the motor drive using the HSG system. The proposed power conversion circuit consists of six insulated gate bipolar transistor (IGBT) modules, a DC-link capacitor, a battery capacitor, an HSG, and seven power relays. Tables 1 and 2 show the volume of the components constituting the conventional HEV and the proposed circuit, respectively. These measured parameters are based on the prototype hardware setup, which was built for this study.

In the case of a conventional HEV, each volume is twice that of the proposed circuit because there are two power converters, namely, a motor drive inverter and an OBC. Although a conventional circuit does not require a DC-link capacitor, the volume of the entire system is 6.295 L.

**Table 1.** Volume of the components of the inverter and on-board charger (OBC) in a conventional hybrid electric vehicle (HEV).

| System Elements     | Volume (L)   |
|---------------------|--------------|
| IGBT modules        | 0.576        |
| Gate driver units   | 0.258        |
| Heat sinks          | 5.036        |
| Sensors             | 0.212        |
| Battery capacitor   | 0.213        |
| Total system volume | 6.295 (100%) |

**Table 2.** Volume of the components in the proposed circuit.

| System Elements     | Volume (L)     |
|---------------------|----------------|
| IGBT modules        | 0.288          |
| Gate driver units   | 0.129          |
| DC-link capacitor   | 0.853          |
| Heat sinks          | 2.518          |
| Sensors             | 0.106          |
| Battery capacitor   | 0.213          |
| Relay               | 0.264          |
| Relay board         | 0.109          |
| Total system volume | 4.480 (71.17%) |

In contrast, the proposed circuit includes half the power components of a conventional circuit, and the total volume is only 4.480 L despite the installation of a power relay, relay board, and a DC-link capacitor. Consequently, the proposed circuit results in a 28% reduction in the volume of the power components. It represents an increase of the power density of about 40% in unit volume. In addition, the manufacturer might save on manufacturing costs by a reduction in production items because the conventional OBC is not needed in the proposed system.

### 2.1. HSG Drive Mode

In the proposed integrated circuit, two different circuit for HSG drive and battery charging mode are configured in accordance with the states of relays as shown in Table 3.

Figure 2a,b show the circuit configuration for different operating modes according to the switching state of the relays. As shown in Figure 2a, the circuit for the HSG drive mode is composed of a battery, a three-phase inverter, and an HSG. When Relay 06 is turned on, the electric energy of the battery is supplied to the three-phase inverter. In this mode, six semiconductors are utilized to configure the conventional three-phase two-level inverter. The DC voltage and current of the battery are converted into AC voltage and current using the three-phase inverter. Relays 03 and 04 are turned on to supply the three-phase AC current to the HSG.

The proposed circuit configuration is also used for regenerative braking. When the vehicle decelerates, the kinetic energy of the vehicle is converted into electric energy using the HSG and three-phase inverter, and the electric energy then charges the battery. Both operations are the same as in a conventional HSG operation.

### 2.2. Bidirectional OBC Mode

The circuit for the bidirectional OBC mode is constructed by reconfiguring the three-phase inverter and HSG, as shown in Figure 2b. To charge the battery, a three-phase inverter is reconstructed into a

single-phase full-bridge AC–DC converter and a DC–DC buck converter. In addition, the winding of the HSG is used as a filter inductor of the DC–DC converter. The equivalent inductance of the filter inductor is 1.5 times that of a single winding in the HSG through the turning on of Relay 05. The proposed power flow control method is achieved when other relays expressed in Figure 2b are turned on. When Relays 01 and 02 are turned on, the single-phase grid system and AC–DC full bridge converter are connected. In addition, Relay 07 is turned on to connect the DC–DC buck converter and the battery.

**Table 3.** The operation mode of the integrated circuit depending on the states of relays.

|                            | Turned on Relays     | Turned off Relays    |
|----------------------------|----------------------|----------------------|
| (a) HSG drive mode         | Relay 03, 04, 06     | Relay 01, 02, 05, 07 |
| (b) Bidirectional OBC mode | Relay 01, 02, 05, 07 | Relay 03, 04, 06     |

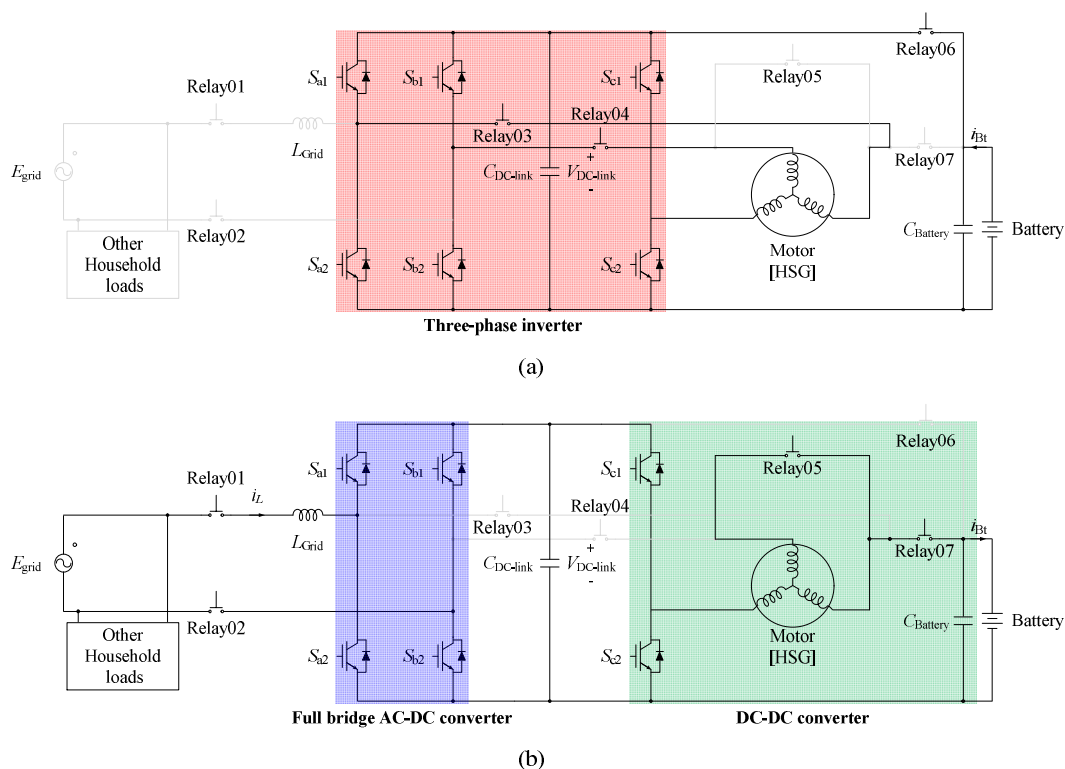


**Figure 2.** Circuit configuration for different operating modes: (a) HSG drive mode and (b) bidirectional OBC mode.

In this topology, the active power is delivered from the grid to the vehicle for charging the battery, and in the opposite direction to supply stored energy in the battery to the grid. Moreover, it is possible to compensate the reactive power, which occurs through the residential load. Compared with a conventional reactive power compensation method, the utilization of the apparent power can be more efficiently improved when located near a residential load. In addition, this method can reduce the maintenance and installation cost used for conventional reactive power compensation because additional facilities are not required.

### 3. Control Method for Battery Charging and Reactive Power Compensation

Figure 3 shows block diagrams of the proposed control methods for the battery charging and compensation of the reactive power. To control the active and reactive powers independently, the grid voltage and current should be expressed in a stationary reference frame. The d-axis voltage and current

are equal to the grid voltage  $E_{grid}$  and inductor current  $i_L$ , respectively. Furthermore, the q-axis voltage and current, which occur using an all-pass filter (APF), are 90-degree delayed signals compared with the d-axis voltage and current. The APF is a signal processing filter that passes all frequencies without changes in magnitude but produces 90-degree phase delay as shown in Figure 4. In this paper, the digital APF is applied using the bilinear transformation method. The transfer functions of an APF on a complex plane and a digital APF using the bilinear transformation method are expressed through the following equations:

$$G_{APF}(s) = \frac{s - \omega}{s + \omega} \tag{1}$$

$$G_{APF}(z) = \frac{(2 - \omega T) - (2 + \omega T)z^{-1}}{(2 + \omega T) - (2 - \omega T)z^{-1}} \tag{2}$$

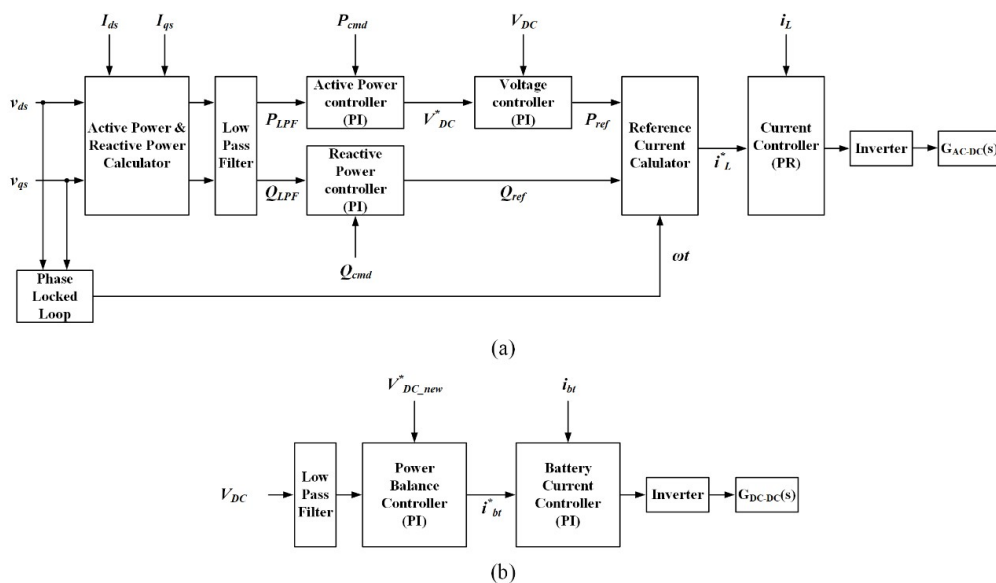


Figure 3. Block diagram of active and reactive power flow control method: (a) AC–DC full bridge converter and (b) DC–DC converter.

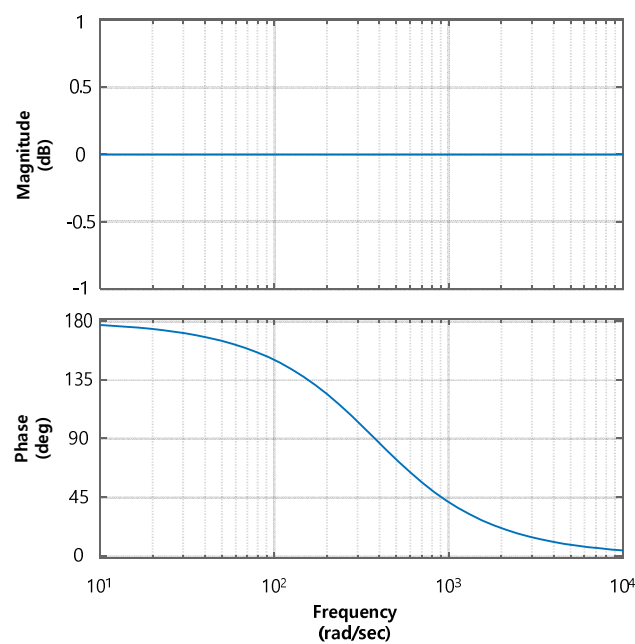


Figure 4. Bode plot of the all-pass filter:  $\omega = 377$  (rad/s).

### 3.1. Control Scheme for AC–DC Full Bridge Converter

Figure 3a shows a control block diagram for an AC–DC full bridge converter. The active and reactive power calculator operates using the measured signals  $v_{ds}$  and  $i_{ds}$ , and the estimated signals  $v_{qs}$  and  $i_{qs}$ . The equations of the active and reactive power calculations are expressed as follows:

$$P = -\frac{1}{2}(v_{ds} \cdot i_{ds} + v_{qs} \cdot i_{qs}) \quad (3)$$

$$Q = \frac{1}{2}(v_{ds} \cdot i_{qs} - v_{qs} \cdot i_{ds}) \quad (4)$$

The calculated active and reactive powers  $P$  and  $Q$  pass through the digital low-pass filter (LPF) as input signals of the active and reactive power controllers, which are composed of a proportional and integral (PI) controller. In an active power controller, the filtered power  $P_{LPF}$  is compared with the active power command  $P_{cmd}$ . In this case,  $P_{cmd}$  can be changed depending on the state of the grid or the demand of the user. The difference between the calculated  $P_{LPF}$  value and the command  $P_{cmd}$  is used as an input signal for the active power controller. Similarly, the difference between the filtered power  $Q_{LPF}$  and the reactive power command  $Q_{cmd}$  is an input signal for the reactive power controller to compensate the reactive power that occurs from the residential inductive load. Contrary to the active power command, reactive power command  $Q_{cmd}$  is only changed depending on the circumstances of the grid.

The active power controller generates voltage reference  $V_{DC}^*$  for the DC-link. The voltage controller regulates the DC-link voltage to supply active power into the battery, depending on the output of the active power controller.

The voltage and reactive power controllers generate active and reactive power references  $P_{ref}$  and  $Q_{ref}$ , respectively. Here,  $P_{ref}$  and  $Q_{ref}$  are used to calculate the reference current signal  $i_L^*$  for the grid current controller. The reference current  $i_L^*$  is calculated using  $P_{ref}$  and  $Q_{ref}$ , and the phase angle of the grid voltage  $\omega t$ . In this paper, the phase angle of the grid  $\omega t$  is estimated using a synchronous reference frame phase-locked loop (SRF-PLL) [24]. The calculation of  $i_L^*$  is expressed through the following equations:

$$\theta = \tan^{-1} \frac{Q_{ref}}{P_{ref}} \quad (5)$$

$$I_L = \frac{P_{ref}}{E_{grid} \cos \theta} \quad (6)$$

$$i_L^* = \sqrt{2} I_L \sin(\omega t - \theta) \quad (7)$$

As shown in Equation (5), the power factor (PF) angle  $\theta$  is expressed using  $P_{ref}$  and  $Q_{ref}$ , which are concluded by the user and grid command. Here,  $I_L$  indicates the root-mean square (RMS) value of the reference current for the battery charging and reactive power compensation. It is calculated using the output of the voltage controller  $P_{ref}$ , the maximum magnitude of grid voltage  $E_{grid}$ , and PF angle  $\theta$ . As a result, the reference signal of inner loop  $i_L^*$  is expressed using the RMS value  $I_L$  and the subtraction between the phase angle of the grid voltage  $\omega t$  and PF angle  $\theta$ , which is expressed in Equation (7).

The grid current controller is composed of a non-ideal proportional resonant (PR) controller. The controller generates a duty ratio  $d_{AC-DC}$ , as shown in the following equation:

$$d_{AC-DC} = K_P \times (i_L^* - i_L) + \frac{2K_R \omega_c s}{s^2 + 2\omega_c s + \omega^2} \times (i_L^* - i_L) \quad (8)$$

where  $K_P$  and  $K_R$  are the proportional and resonance gain, respectively. In addition,  $\omega_c$  is the cut-off frequency, and  $\omega$  is the resonance frequency. The ideal PR controller is vulnerable to variations in the selected frequency owing to the infinite gain and narrow frequency bandwidth characteristics for the selected frequency. In contrast, the non-ideal PR controller has more robust characteristics

regarding the variation in the selected frequency than the ideal-PR controller [25]. The AC–DC full bridge converter conducts its switching operation using the output from the non-ideal PR controller. Consequently, a unipolar modulation is applied to the switching method of the AC–DC full bridge converter, and, therefore, the output voltage has three levels:  $-V_{DC}$ , 0, and  $V_{DC}$ . In the block diagrams shown herein, the function  $G(s)$  indicates the load of each controller.

### 3.2. Control Scheme for DC–DC Converter

Figure 3b shows a block diagram for operation of the DC–DC buck converter. The battery reference current  $i_{bt}^*$  is calculated by amplifying the error between the reference DC-link voltage  $V_{DC\_new}^*$  and instantaneous DC-link voltage  $V_{DC}$ . This controller does not compete against the voltage controller used in the block diagram of the AC–DC full bridge converter but helps it achieve an input–output power balance. The battery current controller, which is composed of a PI controller, creates the duty  $d_{DC-DC}$  based on the following equation:

$$d_{DC-DC} = K_{bt\_P} \times (i_{bt}^* - i_{bt}) + \frac{K_{bt\_I}}{s} \times (i_{bt}^* - i_{bt}) \tag{9}$$

where  $K_{bt\_P}$  is the proportional gain, and  $K_{bt\_I}$  is the integral gain. All controllers used in the system are equipped with an anti-windup to prevent accumulation of the integrator.

## 4. DC Offset Compensation Method

In general, some of the reasons which cause a DC offset include scaling errors of the voltage and current measurement, an undesirable dead time applied in the power conversion devices, and the performance difference between full bridge converter switches. When the grid current or voltage contains the DC offset component, the DC offset component is presented as a ripple component in the rotating coordinate frame. If the input signal contains the ripple component without filtering, the control performance deteriorates. Moreover, various problems occur in the system, such as overheating, deteriorating the efficiency and shortening the battery lifespan.

In this section, a DC offset compensation method is proposed for a vehicular battery charger. The proposed method improves the battery charging performance by eliminating the DC offset component using a digital control without an additional passive element or sensor.

As shown in Figure 5a, the grid current with a DC offset is expressed using the sum of the fundamental wave component  $i_{grid\_fundamental}$  and DC offset component  $I_{grid\_offset}$  expressed through the following equation:

$$i_{grid} = i_{grid\_fundamental} + I_{grid\_offset} \tag{10}$$

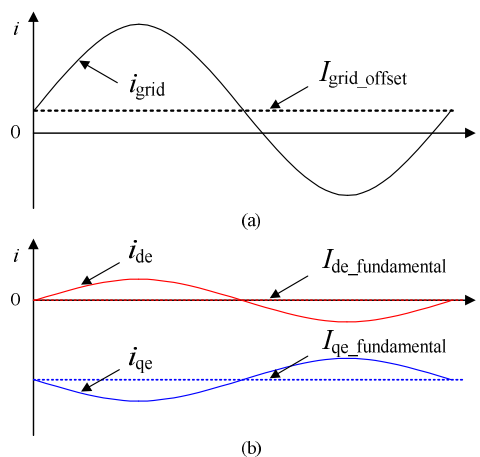


**Figure 5.** Waveform of current with DC offset: (a) Grid current and (b) d–q axis current contained in the DC offset.

Through the coordinate transformation, the grid current is expressed as the value on the d–q axis of the rotating coordinate frame, as shown in the following equations:

$$i_{de} = i_{de\_fundamental} + I_{de\_offset} \tag{11}$$

$$i_{qe} = i_{qe\_fundamental} + I_{qe\_offset} \tag{12}$$

where  $i_{de\_fundamental}$  and  $i_{qe\_fundamental}$  are the DC values indicating the waveform of the fundamental to control,  $i_{de\_offset}$  and  $i_{qe\_offset}$  are the AC values which are compensated by using the proposed method. In the above equations, the AC components have the same frequency as the grid current, as shown in Figure 5b.

Figure 6 shows a block diagram including the DC offset controller and the fundamental wave controller. As shown in the block diagram, each controller is composed of a PI controller. The grid current containing DC offset  $i_{grid}$  is converted into variable  $i_{dqe}$  in the rotating coordinate frame using the APF and a coordinate transformation. Comparing the value between the reference current  $i_{dqe}^*$  and real current on the d–q axis,  $i_{dqe}$  is utilized as the input of the fundamental wave controller. The controller generates the reference voltage  $v_{dqe}^*$  to operate the OBC. The reference voltage for the rotating reference frame  $v_{dqe}^*$  is converted for the stationary reference frame to be used as the input of the inverter.

Moreover, it is possible to detect the AC component having the same frequency as the grid current on the rotating reference frame, using the difference between the actual d–q axis current  $i_{dqe}$  and the reference current  $i_{dqe}^*$ , as shown in the following equations:

$$i_{de\_offset} = i_{de} - i_{de}^* \tag{13}$$

$$i_{qe\_offset} = i_{qe} - i_{qe}^* \tag{14}$$

In Equations (13) and (14), the AC component  $i_{dqe\_offset}$ , which indicates the difference between  $i_{de}^*$  and  $i_{de}$ , and  $i_{qe}^*$  and  $i_{qe}$ , is converted into a DC variable for the stationary reference frame through an inverse transformation. The differences between  $i_{dqs\_offset}$  and  $i_{dqs\_offset}^*$  are used as the inputs of the DC offset controller. The DC offset controller generates reference voltages  $v_{dqs\_offset}^*$  to compensate the DC offset contained in the grid current. Consequently, the sum of the voltages  $V_{dqs}^*$  and  $V_{dqs\_offset}^*$  is compared with the triangular waveform to ensure that the inverter operates stably even though the DC offset is included in the grid current  $i_{grid}$ .

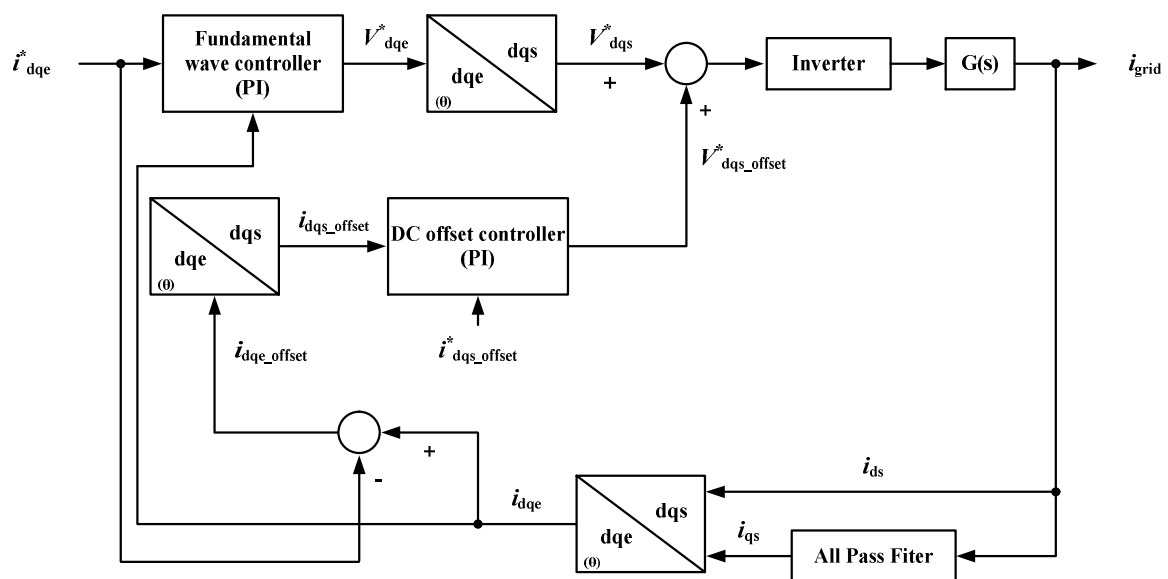


Figure 6. Block diagram of DC offset compensation method.

### 5. Lower-Order Harmonics Compensation Method

In the single-phase grid system, the characteristics of the system and the utilization of the dead time cause lower-order harmonics in the grid current. The lower-order harmonics in grid current result in aggravated power quality and increased heating in the equipment and conductors.

To compensate these lower order harmonic currents, many of the researches have been actively conducted [26,27]. In Reference [26] the design method of the hybrid power filter is proposed. However, the methodology requires additional components, and the designed filter requires independent passive filters for each low-order harmonics. The adaptive dead-time compensation method is proposed in Reference [27]. The compensation algorithm takes a short computational period. However, it is not applicable to a d–q PI controller and requires a complex reference model.

Figure 7 shows a block diagram of the lower-order harmonics compensation method. In this block diagram, a third-order harmonics current is compensated using a non-ideal PR controller. The third-order harmonic is very close to the fundamental component. Therefore, the PR controller is suitable for eliminating the third-order harmonic because of its narrow frequency bandwidth. However, the ideal PR controller has infinite gain and an excessive narrow frequency bandwidth for the selected frequency, therefore, its robustness for frequency variation is poor. The non-ideal PR controller is put forward to improve its bandwidth because it has finite gain and a wider bandwidth compared to the ideal PR controller. Consequently, it is possible to eliminate the third-order harmonic near the fundamental wave without affecting the control of the fundamental frequency. The non-ideal PR controller equation for compensation of the third-order harmonic is derived as Equation (15).

$$v_{ds\_3rd}^* = K_{P\_3rd} \times (i_{ds\_3rd}^* - i_{ds}) + \frac{2K_{R\_3rd}\omega_c s}{s^2 + 2\omega_c s + (h\omega)^2} \times (i_{ds\_3rd}^* - i_{ds}) \tag{15}$$

where  $i_{ds\_3rd}^*$  is the reference current of the PR controller,  $K_{P\_3rd}$  is the proportional gain,  $K_{R\_3rd}$  is the resonance gain,  $\omega_c$  is the cut-off frequency, and  $h\omega$  is the product of the order of the harmonics to compensate and the resonance frequency.

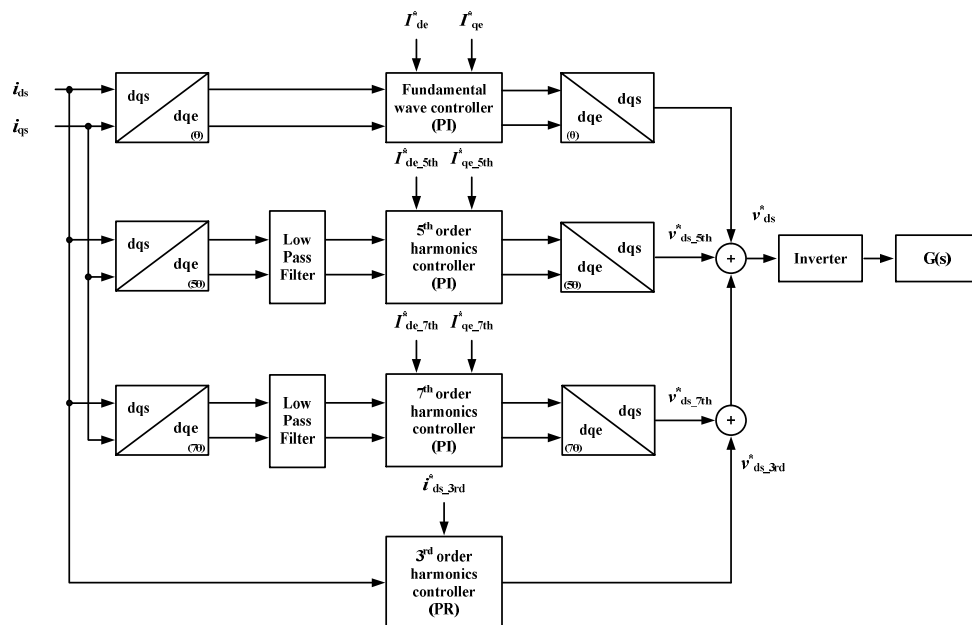


Figure 7. Block diagram for lower-order harmonics compensation method.

The fifth- and seventh-order harmonics currents are compensated using the LPF and PI controllers. Using the grid phase angle calculated from the SRF-PLL, each harmonic current is transformed into

a DC value including the AC component in the d–q axis rotating coordinate frame, as shown in the following equations:

$$\begin{aligned} i_{de\_5th} &= I_{de\_5th\_DC} + i_{de\_5th\_AC} \\ i_{qe\_5th} &= I_{qe\_5th\_DC} + i_{qe\_5th\_AC} \end{aligned} \quad (16)$$

$$\begin{aligned} i_{de\_7th} &= I_{de\_7th\_DC} + i_{de\_7th\_AC} \\ i_{qe\_7th} &= I_{qe\_7th\_DC} + i_{qe\_7th\_AC} \end{aligned} \quad (17)$$

In Equations (16) and (17), only the DC components are extracted from each current component expressed in the d–q axis coordinate frame using the LPF. The filtered value and the harmonic reference current are used as inputs of each order harmonic controller. Consequently, the output of the controller is added to the fundamental reference voltage after an inverse coordinate transform, reducing the lower-order harmonics in the grid current.

## 6. Simulation and Experimental Analysis

### 6.1. Simulation Results

To verify the effective operation of the proposed OBC design and control method, the proposed method was first tested using Powersim, which is a power electronics simulation tool. Considering the resistance existing in the side line of the grid, a small amount of resistance was applied. In the proposed topology shown in Figure 2b, the side inductor of the grid acts as a filter to improve the total harmonic distortion (THD) of the current. Thus, the filter inductor is set at 1.5 mH taking into consideration certain facts, such as the switching frequency. Moreover, the DC-link capacitor is set at 1000  $\mu$ F taking into consideration the overall system volume and second-order ripple of the DC-link current. The filter inductor for the operation of the DC–DC buck converter  $L_{HSG}$  is composed of HSG windings. As a result, the filter inductor of the DC–DC converter is set to approximately 0.9075 mH owing to the HSG windings, which are connected in series and in parallel. The battery capacitor is set at 610  $\mu$ F similar to the set up used in the DC-link capacitor. In the PSIM software, it is impossible to simulate a battery. Because a battery acts as a load in the simulations conducted, the load side resistance was set at 20  $\Omega$  based on the rating of the OBC. The grid voltage used was 220  $V_{rms}$  and varied at 60 Hz. The switching frequency and sampling time were selected as 10 kHz and 100  $\mu$ s, respectively. The DC-link voltage was controlled at 400 V when considering the system efficiency. The detailed simulation parameters are given in Table 4.

**Table 4.** Simulation parameters.

| Parameters                               | Value | Unit      |
|--|-------|-----------|
| Grid side voltage ( $E_{grid}$ )         | 220   | $V_{rms}$ |
| Grid side line resistance ( $R_{grid}$ ) | 0.2   | $\Omega$  |
| Grid side inductance ( $L_{grid}$ )      | 1.5   | mH        |
| DC-link capacitance ( $C_{DC-link}$ )    | 1000  | $\mu$ F   |
| HSG winding inductance ( $L_{HSG}$ )     | 0.605 | mH        |
| Battery capacitance ( $C_{Battery}$ )    | 610   | $\mu$ F   |
| Load resistance ( $R_{battery}$ )        | 20    | $\Omega$  |
| DC-link voltage                          | 400   | V         |
| Switching frequency                      | 10    | kHz       |

Figure 8 shows the simulation results of the active and reactive power flow control method when the referenced active and reactive powers are changed. To confirm that the referenced active and reactive powers are controlled independently, each of the transient states is shown at 0.5 and 0.8 s, respectively. The grid side current is changed owing to the variation in active or reactive power. The variation in active power mainly affects the magnitude of the current, and, thus, the grid side current increases or decreases based on the variation in the active power. In contrast, the variation

in reactive power affects the PF of the grid side current. When the reactive power generated is approximately 3 kVAR, it can be confirmed that the PF is the leading factor.

However, the reactive power is generated at approximately  $-3$  kVAR, and the PF changes from a leading to a lagging factor. Apart from the fluctuation of the active and reactive powers, the DC-link voltage maintains a constant value depending on the reference of the DC-DC side voltage controller, except for the second-order ripple. A battery current only fluctuates when the referenced active power is changed. As the referenced active power is increased, the battery current increases along with the grid side current. Thus, the fluctuation of the referenced active power influences not only the magnitude of the grid side current but also the magnitude of the battery current.

Figure 9 shows the simulation results of the DC offset compensation method. Before the proposed method is applied, a DC offset of approximately 8 A occurs in the grid current. The ripple of the DC-link voltage varies from approximately 364.1 to 434.9 V. Moreover, the offset currents in the rotational coordinate frame d-q axis vary from approximately 10 to  $-15$  A. After the proposed method is applied at 0.4 s, it is possible to observe that the DC offset is eliminated in the grid current. Moreover, the ripple of the DC-link voltage is decreased by approximately 10 V, and, thus, the variation in the DC-link voltage is from 374.9 to 425.3 V. In addition, the variation in the offset currents in the rotational coordinate frame d-q axis is approximately 2 to  $-6$  A.

Figure 10 shows the simulation results without the lower-order harmonics compensation method. If the proposed method is not applied, the THD of the grid current is approximately 8.14%, which is not suitable for the limits of the THD specified by IEC61000, the international standard for an input current. Moreover, the fast Fourier transform (FFT) analysis results indicate that the grid current includes lower-order current harmonics.

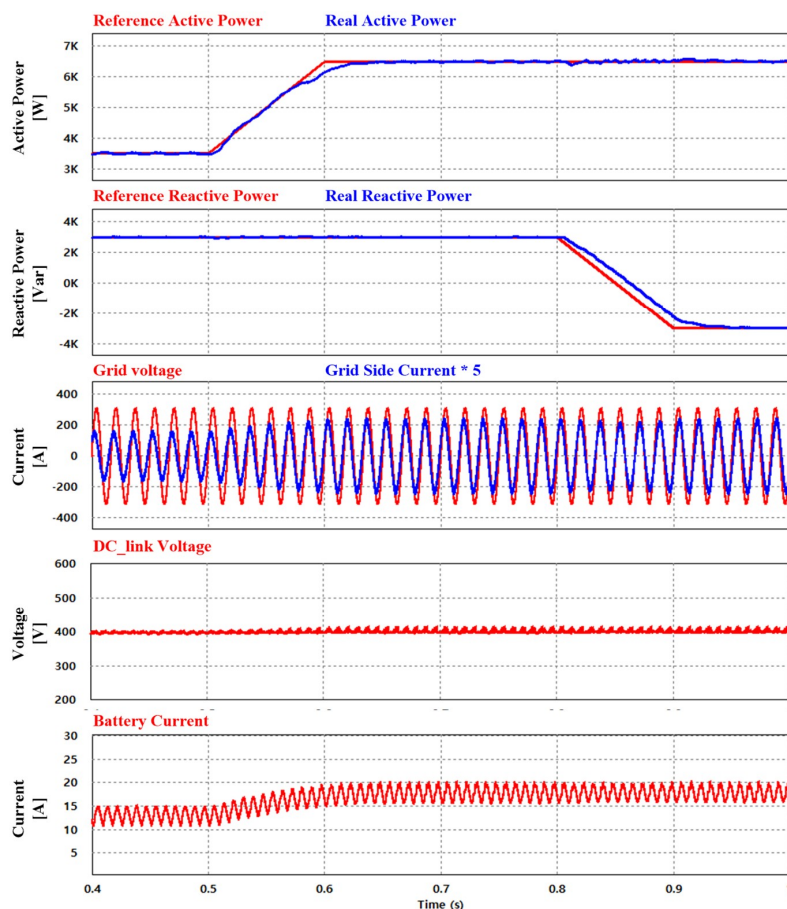


Figure 8. Simulation results of active and reactive power flow control method.

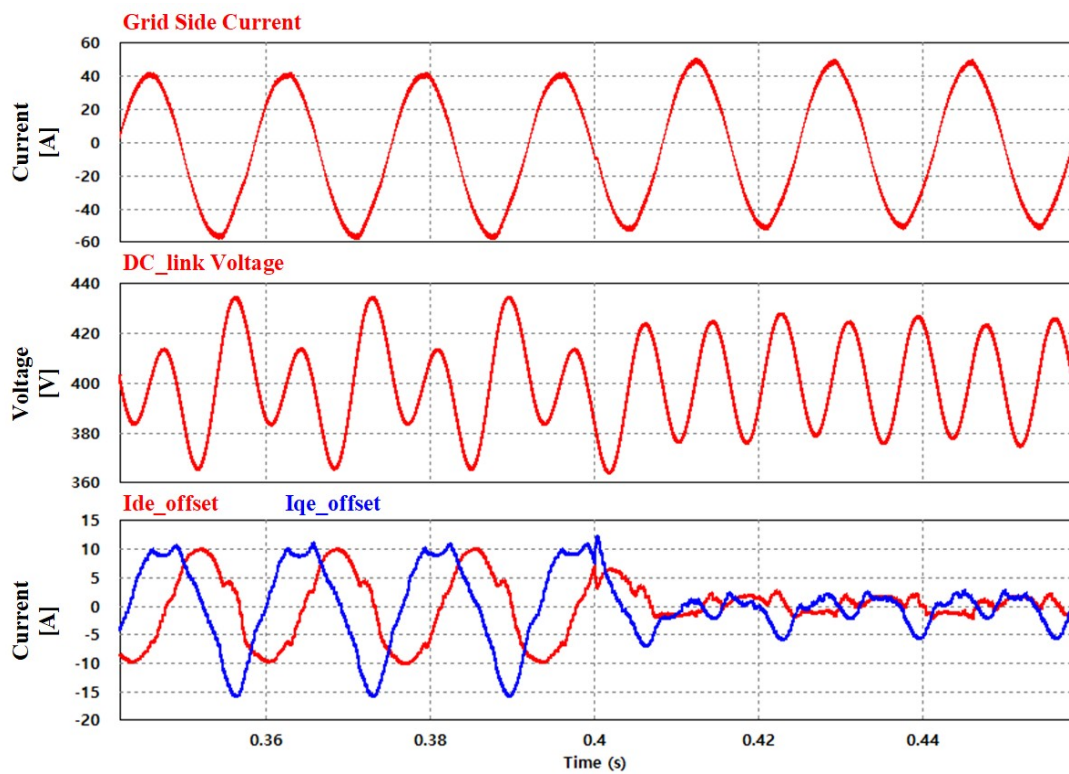


Figure 9. Simulation results of DC offset compensation method.

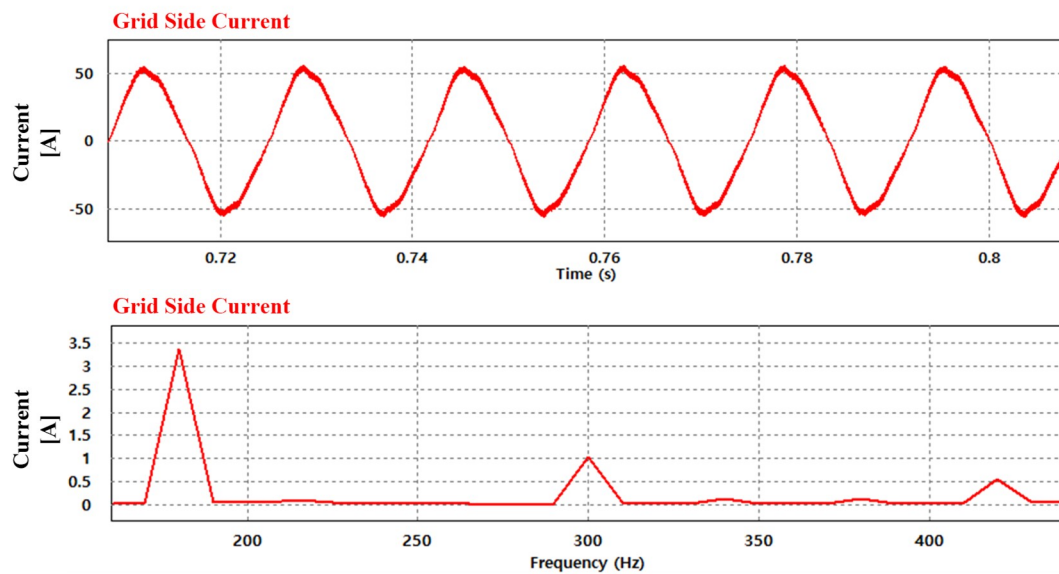
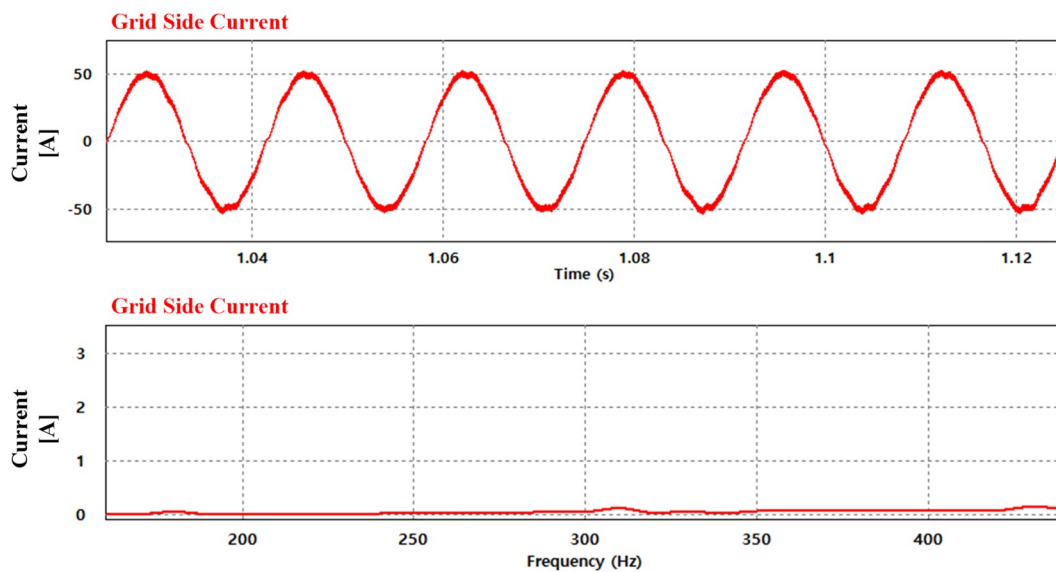


Figure 10. Simulation results without applying lower-order harmonics compensation method.

Figure 11 shows the simulation results when applying the lower-order harmonics compensation method. Compared with the case in which the controller is not operated, it is possible to observe that the waveform of the grid side current is improved. The THD of the current is improved by up to 3.63%. Moreover, it is possible to confirm that the lower-order current harmonics are significantly reduced based on the FFT analysis results.



**Figure 11.** Simulation results when applying lower-order harmonics compensation method.

## 6.2. Experimental Results

Figure 12 shows the practical experimental set construction. The prototype bidirectional OBC consists of a relay board, and control board, etc. The control board consists of a digital signal processor (DSP) TMS320F28335 and other peripherals. Among the motor/generator set, we only use the winding of the HSG operating as a filter inductor of the DC–DC converter. The parameters of the experiment are the same as those of the simulation, as indicated in Table 4.

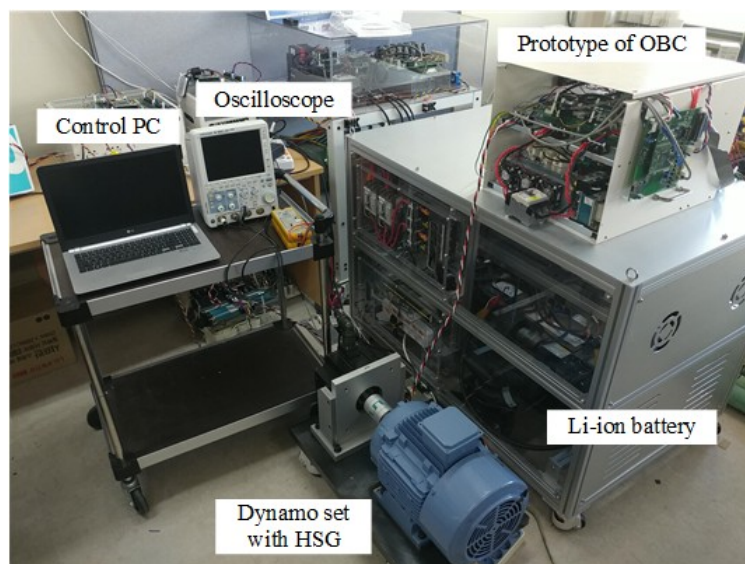


**Figure 12.** Construction of the experiment hardware set.

Figure 13 shows the experimental results of the active and reactive power flow control method. The DC-link voltage is controlled at 400 V, similar to the simulation. As shown in Figure 13a, the reactive power controller produces fast response following the step change of its command. When the reactive power output is 3 kVAR, the grid current shows a leading PF compared with the grid voltage, as shown in Figure 13b. The PF of the grid side current is 0.432, i.e., leading, because the active power is controlled at approximately 6.5 kW. As shown in Figure 13c, the reactive power controller generates

−3 kVAR of reactive power. In this case, the PF is 0.432, i.e., lagging, with the active power, which is controlled at 6.5 kW.

Figure 14 shows the experimental waveforms of the grid side and battery current depending on the increasing of the active power. In this experiment, the active power varies from 3.5 to 6.5 kW as shown in Figure 14a. In contrast, the reactive power is controlled as 0 kVAR. When the controlled active power is 3.5 kW, the magnitude of the grid current is about 35.6 A and the average value of the battery current is approximately 13.2 A as shown in Figure 14b. When the active power is changed to 6.5 kW, the grid side and battery current are increased, as shown in Figure 14c. In this case, the magnitude of the grid current is about 49.5 A and the average value of the battery current is approximately 18.0 A. Because the reactive power is controlled at 0 kVAR, the grid side current shows the unit PF.

Figure 15 shows the experimental results of the DC offset compensation method. In order to confirm the performance of the compensation method clearly, the DC offset current is injected intentionally as shown in the left side of Figure 15a. Since the grid current includes severe DC offset component, which is approximately 6A, the DC-link voltage is fluctuated from 377 to 423 V. In addition, the fluctuation of the DC-link voltage causes the distortion of the grid current as shown in Figure 15b. The proposed compensation method is applied at the middle of the time scale and the DC offset component in the grid current is eliminated as shown in Figure 15c. In addition, the fluctuation of the DC-link voltage is reduced from 382 to 418 V and the grid current is produced as sinusoidal waveform.

Figure 16 shows the experimental results of the lower-order harmonics compensation method. As shown in Figure 16a, the FFT analysis result shows that the grid current contains lower-order harmonics current especially 3rd, 5th, and 7th harmonics. Therefore, the grid side current waveform is distorted by the harmonics. When the proposed compensation method is applied, the FFT analysis result shows that the harmonic currents are eliminated as shown in Figure 16b. In addition, the quality of the grid current is improved by eliminating the harmonic components.

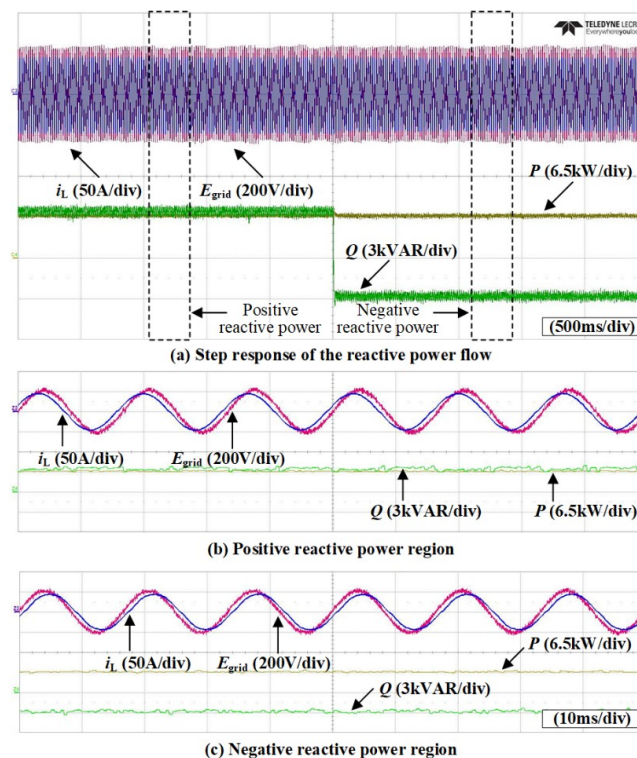


**Figure 13.** Experimental results of active and reactive power flow control method when the power factor changes from leading to lagging: (a) step response of the reactive power, (b) PF = 0.432 leading and (c) PF = 0.432 lagging.

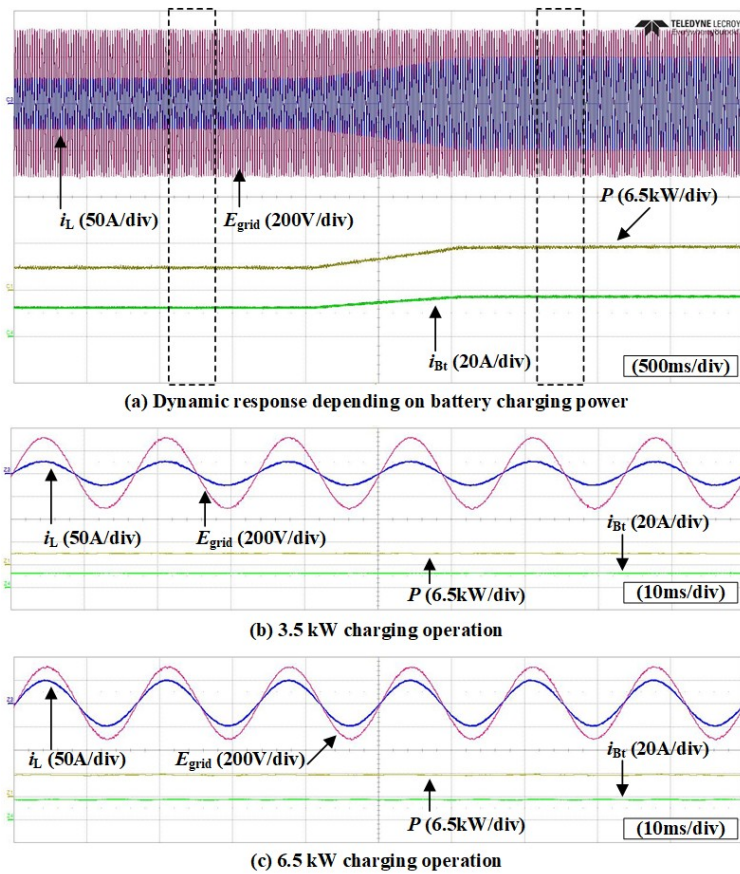


Figure 14. Experimental results of active power and battery current controllers: (a) Variation of the charging power from 3.5 to 6.5 kW, (b) P = 3.5 kW, (c) P = 6.5 kW.

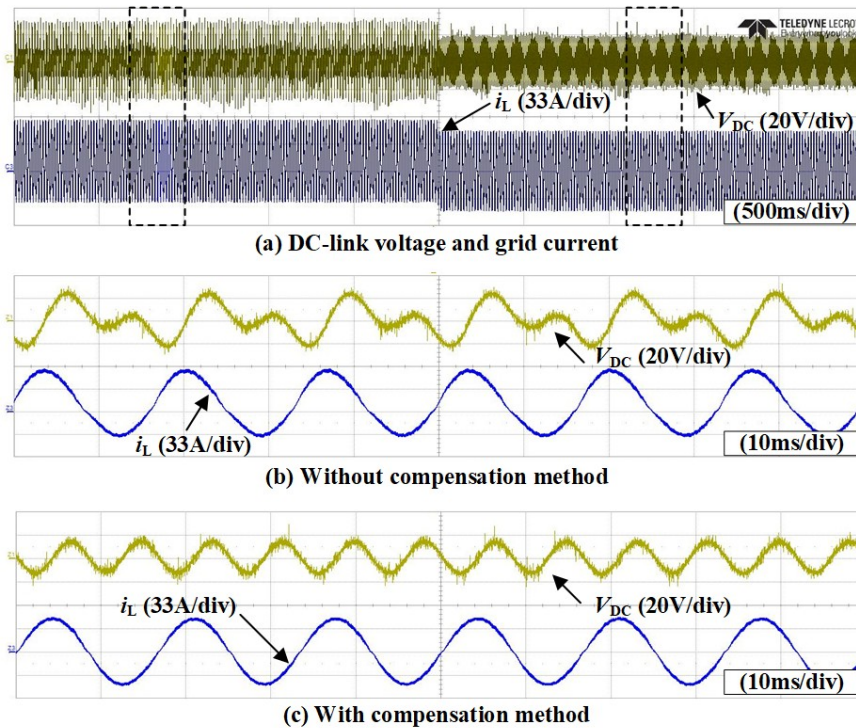
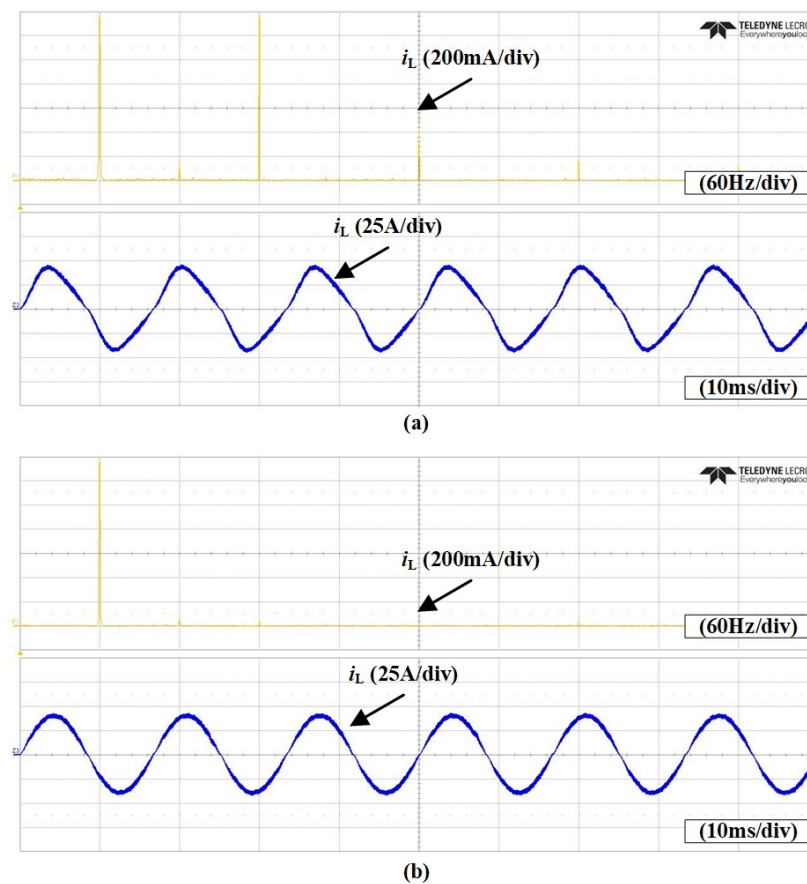


Figure 15. Experimental results of DC offset compensation method: (a) Waveforms of DC-link voltage and grid current, (b) waveforms with DC offset current (c) waveforms with the proposed DC offset compensator.



**Figure 16.** Experimental results of lower-order harmonics compensation method: Waveforms of grid current and FFT analysis (a) without and (b) with the proposed compensation method.

## 7. Conclusions

This paper proposed the design and control method of a single-phase bidirectional OBC using an HSG and an inverter in an HEV. The proposed circuit for HSG operation in an HEV acts as an integrated charging system through the circuit reconfiguration based on the relay states. Therefore, the number of power converters is effectively reduced through the replacement of a conventional OBC, thereby increasing the power density. Moreover, the proposed control method allows for both battery charging and reactive power compensation depending on the user command. In addition, some controllers are added to operate a single-phase bidirectional OBC in a stable manner. The PSIM simulation and experimental results are used to verify the design and control method of the proposed single-phase bidirectional OBC.

**Author Contributions:** K.-B.L. provided guidance and supervision. H.-S.K. conceived the idea of this paper and conducted the simulation. S.-M.K. implemented the main research methodology, conducted the simulation and experiment, wrote the paper, and revised the manuscript. All authors have equally contributed to the simulation analysis, experiment, and discussions on the results.

**Funding:** This work was supported by the Korea Institute of Energy Technology Evaluation and Planning (KETEP) and the Ministry of Trade, Industry and Energy (MOTIE) of the Republic of Korea (No. 20171210201100) and “Human Resources Program in Energy Technology” of the Korea Institute of Energy Technology Evaluation and Planning (KETEP), granted financial resource from the Ministry of Trade, Industry and Energy, Republic of Korea. (No. 20174030201660).

**Acknowledgments:** Authors thank our Power Electronics Laboratory colleagues of Electrical & Computer Engineering Department, Ajou University, South Korea.

**Conflicts of Interest:** The authors declare no conflict of interest.

## References

1. Moreno, J.; Ortuzar, M.E.; Dixon, J.W. Energy-management system for a hybrid electric vehicle using ultracapacitors and neural networks. *IEEE Trans. Ind. Electron.* **2006**, *53*, 614–623. [[CrossRef](#)]
2. Bak, Y.S.; Lee, E.S.; Lee, K.B. Indirect Matrix Converter for Hybrid Electric Vehicle Application with Three-Phase and Single-Phase Outputs. *Energies* **2015**, *8*, 3849–3866. [[CrossRef](#)]
3. Camara, M.B.; Gualous, H.; Gustin, F.; Berthon, A.; Dakyo, B. DC/DC converter design for supercapacitor and battery power management in hybrid vehicle applications—Polynomial control strategy. *IEEE Trans. Ind. Electron.* **2010**, *57*, 587–597. [[CrossRef](#)]
4. Park, H.-S.; Kim, C.-E.; Kim, C.-H.; Moon, G.-W.; Lee, J.-H. A modularized charge equalizer for an HEV lithium-ion battery string. *IEEE Trans. Ind. Electron.* **2009**, *56*, 1464–1476. [[CrossRef](#)]
5. Montazeri-Gh, M.; Soleymani, M. Investigation of the energy regeneration of active suspension system in hybrid electric vehicles. *IEEE Trans. Ind. Electron.* **2010**, *57*, 918–925. [[CrossRef](#)]
6. Weng, K.T.; Pollock, C. Low-cost battery-powered switched reluctance drives with integral battery-charging capability. *IEEE Trans. Ind. Appl.* **2000**, *36*, 1676–1681.
7. Barnes, M.; Pollock, C. Forward converters for dual voltage switched reluctance motor drives. *IEEE Trans. Power Electron.* **2001**, *16*, 83–91. [[CrossRef](#)]
8. Liaw, C.; Chang, H. An integrated driving/charging switched reluctance motor drive using three-phase power module. *IEEE Trans. Ind. Electron.* **2011**, *58*, 1763–1775.
9. Plesko, H.; Biela, J.; Luomi, J.; Kolar, J. Novel concepts for integrating the electric drive and auxiliary DC–DC converter for hybrid vehicles. *IEEE Trans. Power Electron.* **2008**, *23*, 3025–3034. [[CrossRef](#)]
10. Buja, G.; Bertoluzzo, M.; Fontana, C. Reactive power compensation capabilities of V2G-enabled electric vehicles. *IEEE Trans. Power Electron.* **2017**, *32*, 9447–9459. [[CrossRef](#)]
11. Jung, J.W.; Lee, S.H.; Lee, G.H.; Hong, J.P.; Lee, D.H.; Kim, K.N. Reduction design of vibration and noise in IPMSM type integrated starter and generator for HEV. *IEEE Trans. Magn.* **2010**, *46*, 2454–2457. [[CrossRef](#)]
12. Chai, F.; Cui, S.M.; Cheng, S.K. Performance Analysis of Double-Stator Starter Generator for the Hybrid Electric Vehicle. *IEEE Trans. Magn.* **2005**, *41*, 484–487. [[CrossRef](#)]
13. Lee, M.-Y.; Lim, D.H.; Kim, S.C. Evaluation of the Effect of Operating Parameters on Thermal Performance of an Integrated Starter Generator in Hybrid Electric Vehicles. *Energies* **2015**, *8*, 8990–9008. [[CrossRef](#)]
14. Liu, C.; Chau, K.T.; Jiang, J.Z. A permanent-magnet hybrid brushless integrated starter-generator for hybrid electric vehicles. *IEEE Trans. Ind. Electron.* **2010**, *57*, 4055–4064. [[CrossRef](#)]
15. Jeong, H.G.; Lee, K.B. A Controller Design for a Stability Improvement of an On-Board Battery Charger. *J. Electr. Eng. Technol.* **2013**, *8*, 951–958. [[CrossRef](#)]
16. Moon, S.H.; Jou, S.T.; Lee, K.B. Performance Improvement of a Bidirectional DC-DC Converter for Battery Chargers using an LCLC Filter. *J. Electr. Eng. Technol.* **2015**, *10*, 560–573. [[CrossRef](#)]
17. Jeong, H.G.; Lee, K.B. A Controller Design for a Quick Charger System Suitable for Electric Vehicles. *J. Electr. Eng. Technol.* **2013**, *8*, 1122–1130. [[CrossRef](#)]
18. Kisacikoglu, M.C.; Kesler, M.; Tolbert, L.M. Single-phase on-board bidirectional PEV charger for V2G reactive power operation. *IEEE Trans. Smart Grid.* **2015**, *6*, 767–775. [[CrossRef](#)]
19. Jeong, H.G.; Lee, J.H.; Lee, K.B. A 2nd Order Harmonic Compensation Method for Wind Power System Using a PR Controller. *J. Electr. Eng. Technol.* **2013**, *8*, 507–515. [[CrossRef](#)]
20. Trinh, Q.N.; Wang, P.; Tang, Y.; Koh, L.H.; Choo, F.H. Compensation of DC Offset and Scaling Errors in Voltage and Current Measurements of Three-Phase AC/DC Converters. *IEEE Trans. Power Electron.* **2018**, *33*, 5401–5414. [[CrossRef](#)]
21. Lee, J.S.; Hwang, S.-H. DC Offset Error Compensation Algorithm for PR Current Control of a Single-Phase Grid-Tied Inverter. *Energies* **2018**, *11*, 2308. [[CrossRef](#)]
22. Lee, J.S.; Kwak, R.H.; Lee, K.B. Novel Discontinuous PWM Method for a Single-Phase Three-Level Neutral Point Clamped Inverter with Efficiency Improvement and Harmonic Reduction. *IEEE Trans. Power Electron.* **2018**, *33*, 9253–9266. [[CrossRef](#)]
23. Nishikawa, K.; Ikeda, F.; Okamoto, Y.; Yamada, H.; Tanaka, T.; Okamoto, M. Improvement in Harmonic Compensation of a Smart Charger with a Constant DC-Capacitor Voltage-Control-Based Strategy for Electric Vehicles in Single-Phase Three-Wire Distribution Feeders. *Energies* **2018**, *11*, 1604. [[CrossRef](#)]

24. Golestan, S.; Guerrero, J.M. Conventional synchronous reference frame phase-locked loop is an adaptive complex filter. *IEEE Trans. Ind. Electron.* **2015**, *62*, 1679–1682. [[CrossRef](#)]
25. Teodorescu, R.; Blaabjerg, F.; Liserre, M.; Loh, P.C. Proportional-resonant controllers and filters for grid-connected voltage-source converters. *IEEE Proc. Electr. Power Appl.* **2006**, *153*, 750–762. [[CrossRef](#)]
26. Rivas, D.; Moran, L.; Dixon, J.W.; Espinoza, J. Improving passive filter compensation performance with active techniques. *IEEE Trans. Ind. Electron.* **2003**, *50*, 161–169. [[CrossRef](#)]
27. Herran, M.A.; Fischer, J.R.; Gonzalez, S.A.; Judewicz, M.G.; Carrica, D.O. Adaptive dead-time compensation for grid-connected PWM inverters of single-stage PV systems. *IEEE Trans. Power Electron.* **2013**, *28*, 2816–2825. [[CrossRef](#)]



© 2018 by the authors. Licensee MDPI, Basel, Switzerland. This article is an open access article distributed under the terms and conditions of the Creative Commons Attribution (CC BY) license (<http://creativecommons.org/licenses/by/4.0/>).